Chemo-mechanical analysis of lithiation/delithiation of Ni-rich single crystals

Shrinidhi S. Pandurangi[a, c], David S. Hall[b, c], Clare P. Grey[b, c], Vikram S. Deshpande[a, c], Norman A. Fleck[a, c, *]

[a]Cambridge University Engineering Department, Trumpington St., Cambridge, CB2 1PZ, UK

[b]Yusuf Hamied Department of Chemistry, University of Cambridge, Lensfield Rd., Cambridge, CB2 1EW UK

[c]The Faraday Institution, Quad One, Harwell Science and Innovation Campus, Didcot, UK

Abstract

Single crystal, Ni-rich layered lithium metal oxides are promising candidates for next-generation cathodes in lithium-ion batteries. However, these Ni-rich materials display anisotropic swelling and contraction during cycling, and this may lead to the generation of internal stresses and thereby to fracture and capacity loss. In this work, the spatio-temporal evolution of lithium concentration and stress state within a $LiNi_{0.8}Mn_{0.1}Co_{0.1}O_2$ (NMC811) single crystal are predicted using a fully coupled chemo-mechanical model. The stress state in the crystal arises from a non-uniform radial distribution of Li concentration, and from a non-linear dependence of intercalation strain upon lithium concentration. The peak tensile stress is greatest near top-of-charge, due to the high sensitivity of intercalation strain upon lithium occupancy at low concentrations, and the peak tensile stress increases with both cycling rate and particle dimension. Significantly, the predicted peak tensile stress is insufficient to cause basal plane fracture of single crystals when their diameter is below 2.5 μm and the charging and discharging rates are below 5C. This suggests that intraparticle fracture is not a significant degradation mode for well-designed NMC811 single crystals.

Keywords: Li-ion batteries, Ni-rich cathodes, single crystals, chemo-mechanical modelling, fracture, cracking

* Corresponding author
E-mail address: naf1@cam.ac.uk

Introduction

In recent years, there has been an increasing global need to replace internal combustion engines by an electric motor/generator in order to reduce both vehicle emissions and the dependence upon fossil fuels. The rapid advance in Lithium-Ion Battery (LIB) technology makes the LIB viable for energy storage in automobiles. [1] Candidate next-generation cathodes for electric vehicle (EV) batteries contain layered, nickel-rich manganese cobalt oxide (NMC) materials. Compared to the more traditional Lithium Cobalt Oxide ($LiCoO_2$, LCO), nickel-rich NMC ($LiNi_pMn_qCo_rO_2$, where $p+q+r=1$, $p \geq 0.5$) contains less cobalt; this is advantageous as cobalt is a rare and expensive element. Additionally, the mining and use of cobalt brings environmental, economic, and humanitarian risks. [2,3] The alloy $LiNi_{0.8}Mn_{0.1}Co_{0.1}O_2$ (known as NMC811) is one such candidate due to its high specific capacity. [4] However, LIBs that utilise Ni-rich cathode materials have shorter practical lifetimes, an issue that has been described as "an unavoidable challenge". [5]

Polycrystalline agglomerates (termed secondary particles) of single crystals (termed primary particles) are commonly used for Li storage in the cathode of a LIB. However, lithiation and delithiation lead to anisotropic swelling and shrinkage, respectively, of each primary particle within the secondary particle and in order to achieve compatibility of adjacent primary particles, a varying elastic strain field (and associated stress state) is generated from particle to particle. These stresses can be of sufficient tensile magnitude that they induce intergranular cracking and fragmentation of the secondary particles. It has been widely proposed that this mechanism is more significant in Ni-rich cathode materials on account of the greater anisotropic expansions and contractions of the crystallographic unit cell than in lower-Ni-content materials. [6] Recent experimental results have shown considerable improvement in electrochemical performance of the cathode upon replacing polycrystalline agglomerates of NMC primary particles by micron-sized primary particles. [7] This raises the question of whether Ni-rich cathode materials with large primary particle size are prone to mechanical fracture during cycling. For this reason, the present paper focuses on large single crystal particles, and predicts the sensitivity of stress generation within the single crystals to the rate of charge/discharge (as quantified by the so-called C-rate) and to the crystal size.

Most theoretical predictions of cracking in Ni-rich storage materials consider secondary particles. For example, Li et al.[8] performed finite element simulations on spherical NMC811 polycrystalline agglomerates and used cohesive zones to idealise the grain boundaries between

primary particles of random size and shape. They demonstrated that the tensile tractions acting on the grain boundaries are sufficient to induce tensile intergranular fracture.

The absence of grain boundaries in single crystal NMC alleviates the problem of self-stress development associated with grain-to-grain anisotropy. But micro-cracking and glide along crystallographic planes can still occur within each grain, as observed by Bi et al.[9] for NMC76 single crystals. Intragranular cracks have also been observed in single crystal NMC622. [10,11] Currently, it is unclear whether these cracks are generated by internal stresses associated with repeated delithiation and relithiation during cell charging and discharge, respectively. Alternatively, cracks may arise from other processes such as mechanical calendaring during electrode processing, [12] thereby motivating the present study.

Several theoretical models have emerged recently to predict the distribution of lithium concentration and stress state in single crystal storage particles. For example, studies on spinel-structured Lithium Manganese Oxide ($LiMn_2O_4$, LMO) have considered the sensitivity of lithium distribution to particle shape. [13-15] Zhao et al.[16] predicted the stress state and likelihood of particle cracking in single crystal LCO, while Nadkarni et al.[17] analysed the metal-insulator phase transition observed in LCO at a Li occupancy above 50%. Phase-field models were developed to study phase separation of lithium-rich $LiFePO_4$ and lithium-poor $FePO_4$ in olivine-structured lithium iron phosphate (LFP). [18,19] Bi et al.[9] predicted the evolution of stress state within single crystal NMC76 due to lithiation and delithiation; to do so, they assumed a concentration-dependent Young's modulus but ignored the influence of stress upon diffusion.

A numerical investigation is now presented on the lithiation/delithiation response of a single crystal NMC811 particle with realistic material properties and particle sizes (i.e., particles with diameter on the order of a few μm), with the effect of lithiation-induced stresses taken into account, and a diffusion coefficient that depends upon the current degree of lithiation. The required level of complexity is assessed by comparing the predictions of the model with those of classical stress-independent Fickian diffusion and constant diffusivity, as used extensively in the literature (see for example Bi et al.[9]). The objective of the present study is two-fold: (1) predict the stress state and lithium occupancy in a single storage particle during its lithiation and delithiation; and (2) generate a design map to estimate the propensity for particle fracture as a function of particle size and rate of delithiation/lithiation of the cathode. Since our study is concerned with cathodes, we will employ the terminology of 'delithiation/lithiation of the cathode' and refrain from using 'charging/discharging of the battery' to avoid possible confusion.

The outline of the remainder of the paper is as follows. After briefly discussing the governing equations and the numerical method, we present and discuss the simulation results, including the effect of charging rate and crystal size upon level of stress generation. Concluding remarks and a summary of the key results are then given. A list of mathematical symbols used in the model is provided in Table 1.

Table 1 A summary of the parameters of the model

Symbol	Description
H	height of the right circular cylindrical particle
d	diameter of the right circular cylindrical particle
r	radial coordinate
ω	angular coordinate
z	axial coordinate
t	time
$\mathbf{e}_r$	radial unit vector
$\mathbf{e}_\omega$	tangential unit vector
$\mathbf{e}_z$	axial unit vector
$\boldsymbol{x}$	position vector
$\mathbf{O}$	geometric centre of the cylinder
Ω	domain of the circular cylindrical particle
$\mathbf{a}$	crystallographic **a** axis
$\mathbf{b}$	crystallographic **b** axis
$\mathbf{c}$	crystallographic **c** axis
$\mathcal{S}$	curved boundary of the circular cylindrical particle
N_{L}	molar density of lattice sites
N_{Li}	molar density of Li^+
θ	lithium occupancy fraction
$\langle\cdot\rangle$	volume averaged quantity
Q	nominal capacity of NMC particle
$\mathcal{F}$	Helmholtz free energy density
$\boldsymbol{\varepsilon}$	strain tensor
T	temperature

W^{θ}	compositional free energy per unit volume of stress-free homogeneous NMC crystal
W^{EL}	elastic free energy density
$\boldsymbol{\sigma}$	Cauchy stress tensor
$\mathbb{C}$	fourth order elasticity tensor
$\boldsymbol{u}$	displacement vector
$\boldsymbol{\varepsilon}^{EL}$	elastic strain tensor
$\boldsymbol{\varepsilon}^{\theta}$	lattice strain tensor
l_a^{θ}	lattice parameter at occupancy θ along **a** axis
l_b^{θ}	lattice parameter at occupancy θ along **b** axis
l_c^{θ}	lattice parameter at occupancy θ along **c** axis
ε_a^{θ}	lattice strain at occupancy θ along **a** axis
ε_b^{θ}	lattice strain at occupancy θ along **b** axis
ε_c^{θ}	lattice strain at occupancy θ along **c** axis
μ_{Li}^{c}	chemical potential of Li atoms in the cathode
$\mu_{\mathrm{Li}}^{\theta}$	compositional chemical potential of stress-free homogeneous NMC crystal
μ_{Li}^{EL}	chemical potential associated with the elastic free energy density
$\mu_{\mathrm{Li}^+}^{c}$	chemical potential of Li^+ ions in the cathode
N_{e^-}	molar density of electrons
$\mu_{e^-}^{c}$	chemical potential of electrons
ϕ^{c}	electric potential of the cathode particle
F	Faraday constant
μ_{Li}^{a}	chemical potential of Li atoms in the anode
$\mu_{\mathrm{Li}^+}^{a}$	chemical potential of Li^+ ions in the anode
ϕ^{a}	electric potential of the anode particle
V_{oc}	open circuit voltage
$\mathbf{f}$	driving force for the migration of Li^+ in the cathode particle
$\boldsymbol{\nabla}$	spatial gradient operator
$\mathbf{M}$	mobility tensor
$\mathbf{v}_d$	drift velocity of Li^+ ions in the cathode particle
$\mathbf{D}$	diffusivity tensor
R	Universal gas constant
D_{Li}	occupancy-dependent diffusivity in the **ab**-plane

ν	hop rate of Li^+ in the NMC lattice
$\langle r^2 \rangle$	mean-square distance
$\mathbf{J}$	flux of Li^+ in the NMC particle
I_S	electronic current density per unit lateral surface area of the circular cylindrical particle
$\mathbf{n}$	unit normal to $\mathcal{S}$
$\hat{\theta}$	test function for the diffusion equation written in weak form
$\hat{v}$	test function for the equation of chemical potential associated with the elastic free energy written in weak form
dV	elemental volume of Ω
dS	elemental area of $\mathcal{S}$
κ	constant which equals +1 for delithiation and -1 for lithiation
ρ	mass density of NMC crystal
σ_c	axial stress
$\sigma_c^{\max}$	maximum axial stress
ε_{zz}	axial strain
ε_0	spatially uniform axial strain for the generalized plane strain case
F_c	axial force
σ_{rr}	radial stress
$\sigma_{\omega\omega}$	tangential stress
a_0	depth of surface thumbnail crack and the radius of a penny-shaped crack
c_0	width of the surface thumbnail crack
K_{IC}	mode I fracture toughness of NMC
D_0	constant diffusion coefficient in Fickian diffusion
E_z	Young's modulus in z direction
ν_{rz}	Poisson's ratio in the rz-plane

Governing equations and solution methodology

Model description and constitutive assumptions.– Consider an isolated NMC811 single crystal surrounded by a liquid electrolyte. The crystal remains electrically neutral as it is connected to the current collector via the carbon binder of the composite cathode. The electrolyte is not considered explicitly as we only model delithiation/lithiation at constant

current. The storage particles are each idealised by a right-circular cylinder of height H and diameter d, see Fig. 1(a); this is an idealised model of the crystal habit of many NMC811 crystals.[20]

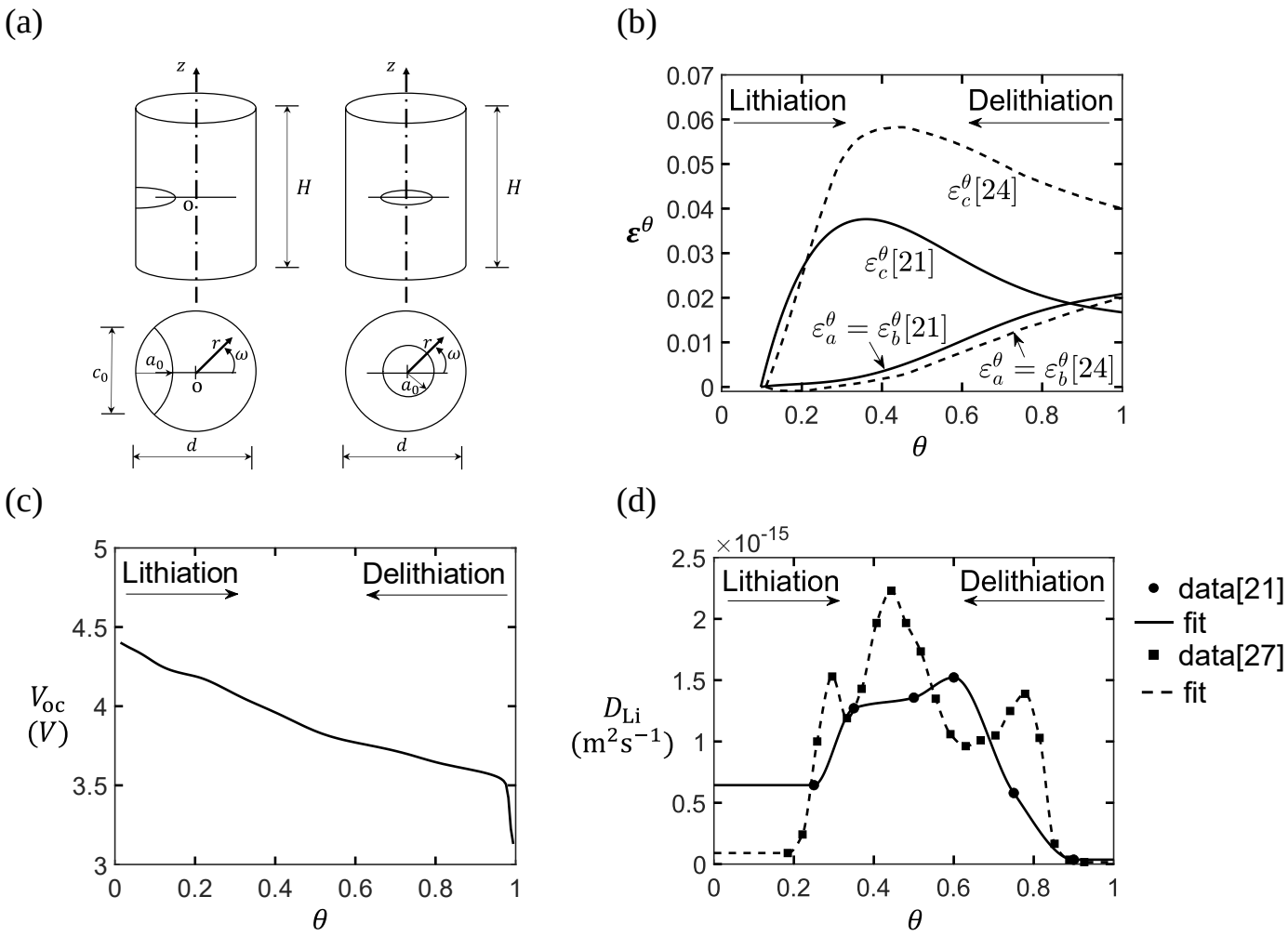

Figure 1. (a) Sketch of the problem analysed. A circular cylindrical particle of height H and diameter d has a surface thumbnail crack of depth a_0 and width c_0 and a penny-shaped centre-crack of radius a_0. (b) lattice strain components $\varepsilon_a^\theta = \varepsilon_b^\theta$ and ε_c^θ, (c) open-circuit voltage V_{oc}[21] and (d) **ab**- plane diffusivity D_{Li} each as a function of Li occupancy θ. The data in (b)-(d) are taken from Refs. 21, 24, 27 as indicated.

Cylindrical coordinates (r, ω, z) and orthonormal base vectors $(\mathbf{e}_r, \mathbf{e}_\omega, \mathbf{e}_z)$ are introduced such that $(\mathbf{e}_r, \mathbf{e}_\omega)$ lie in the crystallographic basal **ab**-plane of the NMC crystal and the axial direction $\boldsymbol{e}_z$ of the cylinder is along the crystallographic **c**-axis of the NMC crystal. The origin **O** of the co-ordinate system is at the geometric centre of the cylinder. The domain of the particle is denoted by Ω and its curved side boundary by $\mathcal{S}$. The layered structure of NMC limits diffusion of lithium ions to occur within the **ab**-plane but not along the **c**-axis. Consequently,

lithium ions enter the particle only over $\mathcal{S}$ during lithiation and vice versa for delithiation. The analysis is simplified by assuming an axisymmetric particle shape and axisymmetric boundary conditions, such that we only need to consider the (r, z) plane.

The unit cell of NMC811 contains three (crystallographically-related) lattice sites for lithium ions that can be simultaneously occupied and is of volume 101 Å^3 in the fully lithiated state.[21] The molar density of lattice sites is $N_{\text{L}} = 49{,}200$ mols m^{-3}. Write $N_{\text{Li}}(\boldsymbol{x}, t)$ as the molar density of Li^+ at a spatial position $\boldsymbol{x} = r\mathbf{e}_r + z\mathbf{e}_z$ at any given time t; then, the lithium occupancy fraction $\theta(\boldsymbol{x}, t)$ is

$$\theta = \frac{N_{\text{Li}}}{N_{\text{L}}}. \qquad [1]$$

Lithium ions diffuse from the particle core to its lateral boundary during delithiation and in the opposite direction during lithiation. At any instant of delithiation/lithiation, the distribution of occupancy within the particle is non-uniform. The state of charge (SOC) at time t is quantified by the average value of lithium occupancy over the volume V of the particle, denoted by $\langle\theta(t)\rangle$, where

$$\langle\theta(t)\rangle = \frac{1}{\text{V}}\int_{\Omega} \theta \; dV. \qquad [2]$$

Assume that the particle is fully lithiated when $\langle\theta\rangle = 0.95$. The nominal capacity of the NMC811 storage particle is $Q = 210$ mAh g^{-1} (assuming that the NMC particle is of density $= 4.78$ g cm^{-3})[22]. This implies that the particle is nominally delithiated when the average occupancy $\langle\theta\rangle = 0.2$

A thermodynamic framework is now introduced for lithium diffusion. Following Onsager[23], the rate of drop of free energy of the system drives dissipation, and so the first step is to determine an expression for the free energy in terms of the strain field and lithium occupancy throughout the crystal. The Helmholtz free energy per unit macroscopic volume of the NMC crystal is written as $\mathcal{F}(\boldsymbol{\varepsilon}, N_{\text{Li}}, T)$ at a temperature T and subjected to a strain $\boldsymbol{\varepsilon}$. Partition the free energy into the compositional free energy per unit volume of a stress-free homogeneous NMC crystal W^{θ} and into the elastic free energy density W^{EL} such that

$$\mathcal{F}(\boldsymbol{\varepsilon}, N_{\text{Li}}, T) = W^{\theta}(\theta) + W^{EL}(\theta, \boldsymbol{\varepsilon}). \qquad [3]$$

Assume a linear elastic response[†] and write the elastic free energy density W^{EL} as

$$W^{EL} = \frac{1}{2}\boldsymbol{\sigma}\colon \boldsymbol{\varepsilon}^{EL}, \qquad [4]$$

where the Cauchy stress tensor $\boldsymbol{\sigma}$ is related to the elastic strain tensor $\boldsymbol{\varepsilon}^{EL}$ through the usual Hooke's law,

$$\boldsymbol{\sigma} = \mathbb{C}\colon \boldsymbol{\varepsilon}^{EL} \qquad [5]$$

and the fourth order elasticity tensor $\mathbb{C}$ denotes the stiffness of the NMC811 crystal. This elasticity tensor possesses the transversely isotropic symmetry of the crystal and is described by five independent components that can, in general, depend upon θ. However, for simplicity, we shall assume that the components of $\mathbb{C}$ are independent of occupancy and employ the values given by Li et al.[8] and are provided in Table 2.

Table 2 Components of $\mathbb{C}$ for the transversely isotropic NMC811 crystal

Component	Value (GPa)
$\mathrm{C}_{rrrr} = \mathrm{C}_{\omega\omega\omega\omega}$	259
$\mathrm{C}_{rr\omega\omega}$	107
$\mathrm{C}_{rrzz} = \mathrm{C}_{\omega\omega zz}$	75
C_{zzzz}	194
$\mathrm{C}_{rzrz} = \mathrm{C}_{\omega z\omega z}$	59

The total strain $\boldsymbol{\varepsilon}$ is derived from the displacement vector field $\boldsymbol{u}(\boldsymbol{x}, t) = (u_r, u_\omega, u_z)$ by

$$\boldsymbol{\varepsilon} = \frac{1}{2}[\nabla\boldsymbol{u} + \nabla\boldsymbol{u}^{\mathrm{T}}]. \qquad [6]$$

In the context of a small strain theory, the total strain $\boldsymbol{\varepsilon}$ is decomposed into the sum of the elastic strain $\boldsymbol{\varepsilon}^{EL}$ and the lattice strain $\boldsymbol{\varepsilon}^{\theta}$ due to intercalation of lithium ions in the NMC811 unit cell such that

$$\boldsymbol{\varepsilon} = \boldsymbol{\varepsilon}^{EL} + \boldsymbol{\varepsilon}^{\theta}. \qquad [7]$$

Now express the components of $\boldsymbol{\varepsilon}^{\theta}$ in the crystal's coordinate system:

[†] Our formulation neglects plasticity and this is justified *a posteriori*.

$$\boldsymbol{\varepsilon}^{\theta} = \begin{bmatrix} \varepsilon_a^{\theta} & 0 & 0 \\ 0 & \varepsilon_b^{\theta} & 0 \\ 0 & 0 & \varepsilon_c^{\theta} \end{bmatrix}. \qquad [8]$$

The components of lithiation strain $\boldsymbol{\varepsilon}^{\theta}$ are determined as a function of lithium occupancy via the experimentally obtained lattice parameters $l_a^{\theta} = l_b^{\theta}$ and l_c^{θ} along the three crystallographic directions. For NMC811, the lattice parameters are taken from Märker et al.[21] and Biasi et al.[24]. Assume that the lattice parameters at an occupancy of $\theta = 0.1$ are the reference values such that all components of $\boldsymbol{\varepsilon}^{\theta}$ vanish at this value of occupancy; consequently, $\boldsymbol{\varepsilon}^{\theta}$ is given by

$$\varepsilon_a^{\theta} = \frac{\Delta l_a^{\theta}}{l_a^{\theta=0.1}} = \frac{l_a^{\theta} - l_a^{\theta=0.1}}{l_a^{\theta=0.1}}, \qquad \varepsilon_b^{\theta} = \varepsilon_a^{\theta}, \qquad \varepsilon_c^{\theta} = \frac{\Delta l_c^{\theta}}{l_c^{\theta=0.1}} = \frac{l_c^{\theta} - l_c^{\theta=0.1}}{l_c^{\theta=0.1}}. \qquad [9]$$

A polynomial regression is used to obtain the functional dependence of $\boldsymbol{\varepsilon}^{\theta}$ upon θ, as shown in Fig. 1(b) for the measured components[21,24] of lattice strain $\varepsilon_b^{\theta} = \varepsilon_a^{\theta}$ and ε_c^{θ}. The lithiation strain components in the **ab**- plane increase monotonically with increasing occupancy and the measurements of Märker et al.[21] and Biasi et al.[24] are in good agreement. The strain component along the **c**-axis first increases steeply up to an occupancy of $\theta = 0.37$ and then decreases as the crystal approaches the fully lithiated state. However, the measurements from the two references are in poor agreement, and this is particularly the case for the peak value of ε_c^{θ} and the strain at high occupancy. Unless otherwise stated, all calculations below use the data of Märker et al.[21] in preference to that of Biasi et al.[24].

We proceed to obtain the governing equations for lithium occupancy as a function of space and time by rewriting the Helmholtz free energy Eq. [3] as

$$\mathcal{F}(\boldsymbol{\varepsilon}, N_{\mathrm{Li}}, T) = W^{\theta}(\theta) + \frac{1}{2}\left[\mathbb{C}\colon\left(\boldsymbol{\varepsilon} - \boldsymbol{\varepsilon}^{\theta}\right)\right]\colon\left(\boldsymbol{\varepsilon} - \boldsymbol{\varepsilon}^{\theta}\right) \qquad [10]$$

upon making suitable use of Eqs. [4], [5] and [7]. The chemical potential of Li atoms in the cathode μ_{Li}^{c} (where the superscript c denotes cathode) is obtained by taking the partial derivative of $\mathcal{F}$ with respect to N_{Li} while holding $\boldsymbol{\varepsilon}$ and T constant, to give

$$\mu_{\mathrm{Li}}^{c} = \frac{1}{N_{\mathrm{L}}}\frac{\partial \mathcal{F}}{\partial \theta} = \mu_{\mathrm{Li}}^{\theta}(\theta) + \mu_{\mathrm{Li}}^{EL}(\theta, \boldsymbol{\varepsilon}), \qquad [11]$$

where $\mu_{\mathrm{Li}}^{\theta}(\theta)$ is

$$\mu_{\mathrm{Li}}^{\theta}(\theta) \equiv \frac{1}{N_{\mathrm{L}}}\frac{\partial W^{\theta}}{\partial \theta} \qquad [12]$$

and $\mu_{\mathrm{Li}}^{EL}(\theta, \boldsymbol{\varepsilon})$ is

$$\mu_{\mathrm{Li}}^{EL}(\theta,\boldsymbol{\varepsilon}) \equiv -\frac{1}{N_L}\left[\mathbb{C}:\left(\boldsymbol{\varepsilon}-\boldsymbol{\varepsilon}^{\theta}\right)\right]:\frac{\partial \boldsymbol{\varepsilon}^{\theta}}{\partial \theta}. \quad [13]$$

Delithiation/lithiation is associated with the flux of Li^+ ions but the crystal remains neutral due to a counter flux of electrons from the current collector. The chemical potential $\mu_{\mathrm{Li}^+}^{c}$ of Li^+ ions in the electroneutral NMC811 crystal is obtained by taking the partial derivative of $\mathcal{F}$ with respect to N_{Li^+} at constant $\boldsymbol{\varepsilon}$ and T. To do so, first recall that the addition of a neutral Li atom is equivalent to adding an Li^+ ion and an electron such that

$$\mu_{\mathrm{Li}}^{c} = \frac{\partial \mathcal{F}}{\partial N_{\mathrm{Li}}} = \frac{\partial \mathcal{F}}{\partial N_{\mathrm{Li}^+}}\frac{\partial N_{\mathrm{Li}^+}}{\partial N_{\mathrm{Li}}} + \frac{\partial \mathcal{F}}{\partial N_{\mathrm{e}^-}}\frac{\partial N_{\mathrm{e}^-}}{\partial N_{\mathrm{Li}}}. \quad [14]$$

where N_{e^-} denotes the moles of electrons. Electroneutrality of NMC811 requires that the differentiation in Eq. [14] is carried out under the constraint $N_{\mathrm{Li}} = N_{\mathrm{Li}^+} = N_{\mathrm{e}^-}$. Upon defining the chemical potential of electrons (Fermi level) by $\mu_{e^-}^{c} \equiv \partial\mathcal{F}/\partial N_{e^-}$, Eq. [14] can be simplified to

$$\mu_{\mathrm{Li}^+}^{c} = \mu_{\mathrm{Li}}^{c} - \mu_{e^-}^{c}. \quad [15]$$

Assume that the Fermi level $\mu_{e^-}^{c}$ of the NMC811 particle is independent of θ and depends only on the electric potential ϕ^c of the cathode particle such that $\mu_{e^-}^{c} = -F\phi^c$, where F is the Faraday constant. Then, the chemical potential for Li^+ ions is determined from Eqs. [11] and [15] to give

$$\mu_{\mathrm{Li}^+}^{c} = \mu_{\mathrm{Li}}^{\theta}(\theta) + \mu_{\mathrm{Li}}^{EL}(\theta,\boldsymbol{\varepsilon}) + F\phi^c. \quad [16]$$

The chemical potential $\mu_{\mathrm{Li}}^{\theta}(\theta)$ is deduced from the open-circuit voltage V_{oc} versus occupancy profile as measured in a Galvanostatic intermittent titration technique (GITT) experiment[21] (see Fig. 1(c)). The GITT experiment is performed on a cell having an NMC cathode and lithium metal anode. The chemical potential of the lithium metal in the stress-free anode is given by a relation analogous to Eq. [16] but with the compositional chemical potential μ_{Li}^{a} now a constant since the occupancy of Li in the metal anode is fixed. We thus write the chemical potential of the Li ions in the anode as

$$\mu_{\mathrm{Li}^+}^{a} = \mu_{\mathrm{Li}}^{a} + F\phi^a \quad [17]$$

where the superscript a denotes anode and ϕ^a is the electrical potential of the anode. In the GITT experiments, open-circuit conditions for the cell are achieved by switching off the external current supply and allowing the lithium ions in the cell to attain electrochemical

equilibrium. In this state, the chemical potentials of the Li ions in the cathode and the anode are equal:

$$\mu^c_{\mathrm{Li}^+} = \mu^a_{\mathrm{Li}^+} \Rightarrow \mu^\theta_{\mathrm{Li}}(\theta) = -FV_{oc}(\theta) + \mu^a_{\mathrm{Li}}, \qquad [18]$$

where $V_{oc}(\theta) \equiv \phi^c - \phi^a$ is the cathode occupancy-dependent open-circuit voltage. The chemical potential $\mu^\theta_{\mathrm{Li}}(\theta)$ obtained using Eq. [18] implicitly accounts for the enthalpic and entropic contributions associated with mixing of Li^+ in the NMC lattice. Upon making use of Eqs. [16] and [18] the chemical potential of Li^+ ions in the cathode reads

$$\mu^c_{\mathrm{Li}^+} = -FV_{oc}(\theta) + \mu^{EL}_{\mathrm{Li}}(\theta, \boldsymbol{\varepsilon}) + \mu^a_{\mathrm{Li}} + F\phi^c\,. \qquad [19]$$

The driving force for migration of the Li^+ ions is obtained from the spatial gradient of the chemical potential, $\mathbf{f} = -\boldsymbol{\nabla}\mu^c_{\mathrm{Li}^+}$. Assume that the drift velocity is proportional to the driving force with a proportionality constant given by the mobility tensor $\mathbf{M}$, i.e., $\mathbf{v}_d = \mathbf{M}\cdot\mathbf{f}$. To ensure positive dissipation, we require that $\mathbf{M}$ is positive definite and symmetric[25] $\mathbf{M} = \mathbf{M}^{\mathrm{T}}$. The diffusivity tensor $\mathbf{D}$ is related to $\mathbf{M}$ in the usual manner by the Stokes-Einstein relation $\mathbf{D} = RT\mathbf{M}$, where R is the gas constant. The layered structure of NMC allows lithium diffusion only within the basal plane, and the diffusivity is treated as isotropic within the basal plane. Upon denoting the occupancy-dependent diffusivity within the basal plane by D_{Li}, the transversely isotropic $\mathbf{D}$ in the crystallographic basis is given by

$$\mathbf{D} = \begin{bmatrix} D_{\mathrm{Li}} & 0 & 0 \\ 0 & D_{\mathrm{Li}} & 0 \\ 0 & 0 & 0 \end{bmatrix}. \qquad [20]$$

We proceed to deduce the magnitude of $D_{\mathrm{Li}}(\theta)$ from two separate types of measurements, as follows. First, deduce $D_{\mathrm{Li}}(\theta)$ from the occupancy-dependent hop rate $\nu(\theta)$ of Li^+ ions in the NMC lattice as obtained by NMR.[21] Isotropic diffusion in the two dimensional (2D) basal plane implies that

$$D_{\mathrm{Li}} = 0.25\nu\langle r^2\rangle\,, \qquad [21]$$

where $\langle r^2\rangle$ is the mean-square distance that the Li^+ ion travels per hop. See for example Böhmer et al.[26] which links NMR measured hop rate to the diffusion coefficient. Now write $\langle r^2\rangle = \left(l^\theta_a\right)^2$ where l^θ_a is the occupancy-dependent lattice parameter in the **ab**-plane. The NMR-derived hopping rate and the lithiation strains (Fig. 1(b)) give a discrete set of diffusivity data as shown in Fig. 1(d), and piecewise cubic interpolation functions are used to curve-fit to

the measured data points. Note that, in the absence of additional data, the diffusivity for $0 \leq \theta \leq 0.25$ and $0.9 \leq \theta \leq 1$ are taken to be constant, with values 0.64×10^{-15} $\mathrm{m^2\,s^{-1}}$ and 0.036×10^{-15} $\mathrm{m^2\,s^{-1}}$, respectively.

Second, use the Galvanostatic polarization and relaxation measurements from Trevisanello et al.[27] to infer the occupancy dependent $D_{\mathrm{Li}}(\theta)$; these data are included in Fig. 1(d) where piecewise cubic interpolation functions are used to curve-fit to the measured data points. Moreover, similar to the first method, we have assumed that the diffusion coefficient is constant over the ranges $0 \leq \theta \leq 0.2$ and $0.9 \leq \theta \leq 1$. Unless otherwise stated, all calculations below make use of the data of Märker et al.[21] in preference to the inferred values from Trevisanello et al.[27].

The flux of $\mathrm{Li^+}$ in the particle is given by $\mathbf{J} = N_{\mathrm{Li^+}}\mathbf{v}_d = -\theta N_{\mathrm{L}}\mathbf{M}\cdot\boldsymbol{\nabla}\mu^c_{\mathrm{Li^+}}$ so that

$$\mathbf{J} = \frac{N_{\mathrm{L}}}{RT}\theta\mathbf{D}\cdot\left[F\frac{\partial V_{oc}}{\partial\theta}\boldsymbol{\nabla}\theta - \boldsymbol{\nabla}\mu^{EL}_{\mathrm{Li}}\right], \qquad [22]$$

where we have used the fact that μ^a_{Li} is constant and the spatial gradient of ϕ^c vanishes as we assume that NMC811 is a good electronic conductor. An additional outcome of this feature is that lithium-ion mobility is not significantly inhibited by Coulombic interactions with what otherwise would be sluggish paired electrons.

Now complete the formulation of the model by rewriting the balance laws in the form of partial differential equations with initial and boundary conditions. Mass balance for the lithium ions demands that the rate of change of $\mathrm{Li^+}$ ions with time t within the particle is given by

$$\frac{\partial N_{\mathrm{Li^+}}}{\partial t} = -\boldsymbol{\nabla}\cdot\mathbf{J} = -\frac{N_{\mathrm{L}}}{RT}\boldsymbol{\nabla}\cdot\left[F\frac{\partial V_{oc}}{\partial\theta}\theta\mathbf{D}\cdot\boldsymbol{\nabla}\theta - \theta\mathbf{D}\cdot\boldsymbol{\nabla}\mu^{EL}_{\mathrm{Li}}\right] \text{ in } \Omega. \qquad [23]$$

This formulation correctly gives Fickian diffusion in the dilute limit of small θ and vanishing $\boldsymbol{\varepsilon^{\theta}}$.

Each storage particle is treated as independent and surrounded by electrolyte. Consequently, a constant ionic flux $\mathbf{J}$ is imposed normal to the lateral surface $\mathcal{S}$ of the particle and is directly related to the electronic current density per unit area $I_{\mathcal{S}}$ by

$$\mathbf{J}\cdot\ \mathbf{n} = \frac{I_{\mathcal{S}}}{F} \text{ on } \mathcal{S}, t \geq 0, \qquad [24]$$

where $\mathbf{n}(\boldsymbol{x})$ is the unit normal to $\mathcal{S}$ at a spatial position $\boldsymbol{x}$.

Assume that the occupancy of the particle is spatially uniform at the beginning of delithiation or lithiation, such that

$$\theta(\boldsymbol{x}, t=0) = \begin{cases} 0.95 & \text{prior to delithiation} \\ 0.2 & \text{prior to lithiation.} \end{cases} \quad [25]$$

Quasi-static conditions for mechanical equilibrium prevail so that

$$\boldsymbol{\nabla} \cdot \boldsymbol{\sigma} = \mathbf{0} \text{ in } \Omega. \quad [26]$$

The external surface of the particle is taken to be free of mechanical tractions, and so

$$\boldsymbol{\sigma} \cdot \mathbf{n} = \mathbf{0} \text{ on } \mathcal{S}, t \geq 0. \quad [27]$$

The physical interpretation is that the particle is free of mechanical constraints arising from neighbouring particles and from the binder. The initial displacement field is such that, at the start of delithiation/lithiation, the particle is stress-free.

We emphasise that the above coupled model treats the NMC particle as a non-ideal mixture of lithium and NMC. Preliminary calculations were performed by assuming an ideal mixture in the coupled model, but with the nonlinear properties of Figs. 1(b) and 1(d). It was discovered that, for realistic values of C-rate and particle size, diffusion arrested prematurely prior to achieving equilibrium. This is unphysical, and emphasises the need for using the above non-ideal mixture theory with a non-linear V_{oc} curve of the type shown in Fig. 1(c).

Numerical Method.– The governing equations are solved by first writing them in weak form and then by making use of the finite element method. Rewrite the mass balance law Eq. [23] by multiplying it with a test function $\hat{\theta}$ and integrating over the particle volume to give

$$\int_{\Omega} \left(N_{\mathrm{L}} \frac{\partial \theta}{\partial t} + \boldsymbol{\nabla} \cdot \mathbf{J} \right) \hat{\theta} \, dV = 0. \quad [28]$$

Then integrate by parts and use the divergence theorem to obtain

$$\int_{\Omega} \left(N_{\mathrm{L}} \frac{\partial \theta}{\partial t} \hat{\theta} - \mathbf{J} \cdot \boldsymbol{\nabla} \hat{\theta} \right) dV + \int_{\mathcal{S}} \mathbf{J} \cdot \mathbf{n} \, \hat{\theta} \, dS = 0. \quad [29]$$

Upon substituting Eq. [22] into [29], the weak form for the mass balance equation reduces to

$$\int_{\Omega} \left(N_{\mathrm{L}} \frac{\partial \theta}{\partial t} \hat{\theta} - \frac{N_{\mathrm{L}}}{RT} \theta \mathbf{D} \cdot \left[F \frac{\partial V_{oc}}{\partial \theta} \boldsymbol{\nabla} \theta - \boldsymbol{\nabla} \mu_{\mathrm{Li}}^{EL} \right] \cdot \boldsymbol{\nabla} \hat{\theta} \right) dV + \int_{\mathcal{S}} \frac{I_{\mathcal{S}}}{F} \hat{\theta} \, dS = 0, \quad [30]$$

where $I_{\mathcal{S}}/F = \mathbf{J} \cdot \mathbf{n}$ is the current flux on $\mathcal{S}$. Note that direct substitution of Eq. [13] for μ_{Li}^{EL} into Eq. [30] gives rise to gradients of stress, and consequently to the presence of a second gradient in displacement field $\boldsymbol{u}$. To avoid working with C^1 (continuously differentiable) interpolation functions for $\boldsymbol{u}$, we follow the approach of Guduru and Bower[28] and adopt a

mixed finite element formulation by treating μ_{Li}^{EL} as an additional degree of freedom which satisfies Eq. [13]. The relevant weak form is obtained by multiplying Eq. [13] by a test function $\hat{v}$ and by integrating the resulting equation over the domain Ω:

$$\int_{\Omega}\left(\mu_{\mathrm{Li}}^{EL}+\frac{1}{N_{\mathrm{L}}}\left[\mathbb{C}\colon\left(\frac{1}{2}\left(\nabla\boldsymbol{u}+\nabla\boldsymbol{u}^{\mathrm{T}}\right)-\boldsymbol{\varepsilon}^{\theta}\right)\right]\colon\frac{\partial\boldsymbol{\varepsilon}^{\theta}}{\partial\theta}\right)\hat{v}\,dV\;=0. \qquad [31]$$

Throughout this study attention is limited to circular cylindrical particles with the **ab** crystallographic plane perpendicular to the axis of the cylinder. Since axisymmetric boundary conditions are imposed the solution is rotationally symmetric within the **ab**-plane such that $u_{\omega}=0$ and the derivatives of all field variables with respect to ω vanish. The governing equations Eqs. [30] and [31] are written in axisymmetric form and are implemented using the 'Weak form PDE' module in COMSOL Multiphysics® (v5.6) coupled with the 'Solid Mechanics' module for the solution of Eqs. [26] and [27]. Built-in solvers for Newton's method are employed, along with a Backward Differentiation Formula (BDF) for the time-stepping algorithm.

Note that the above formulation gives the possibility of θ laying outside the physical range 0 to 1. However, for realistic choice of particle sizes and C-rates we find that the numerical formulation gives $0\leq\theta\leq1$.

Results

Before we report and discuss the results it is appropriate to relate the electronic current density per unit surface area I_S to the common definition of charging and discharging rate of a battery, known as the C-rate. By definition, a C-rate of nC indicates that a current is applied to the electrode – or here a cathode particle – such that it nominally delithiates (or fully lithiates) in $(1/n)$ hours. The value of I_S required to delithiate (or lithiate) a circular cylindrical particle of diameter d at a nC-rate is given by

$$I_S=\kappa\rho n dQ/4, \qquad [32]$$

where $\kappa=+1$ for delithiation, $\kappa=-1$ for lithiation, $\rho=4.78\ \mathrm{g\ cm^{-3}}$ is the density of NMC and $Q=210\ \mathrm{mAh\ g^{-1}}$ is the nominal practical capacity of NMC811. Thus, to simulate lithiation or delithiation at a nC-rate we impose a constant finite current Eq. [32] over the time interval $0\leq t\leq1/n$, followed by $I_S=0$ for $t>1/n$. We emphasise that, at $t>1/n$, lithium continues to diffuse within the particle until equilibrium is reached such that the particle attains a spatially uniform Li occupancy θ and becomes both stress-free.

The remainder of this section is as follows. We begin by discussing the results for delithiation and lithiation of a particle of diameter 2 μm with a fast charging rate of 4C. We consider first a particle of height $H = d$ with $d = 2$ μm, and then consider two limiting values of cylinder aspect ratio H/d : (i) a long cylindrical particle, $H/d \to \infty$, and (ii) a disc shaped particle, $H/d \to 0$. Contours of maximum tensile stress are plotted as a function of C-rate and particle diameter, where the maximum values have been obtained over both time and space. Variability exists in the diffusivity and lithiation strain data, recall Fig. 1 where the data of Märker et al.[21] are compared with that of Refs. 24, 27. The effects of this variability upon the predicted time-evolution of occupancy and stress are discussed in the subsection entitled 'Effect of the uncertainty of the non-linear parameters'. Finally, we investigate the importance of using the fully-coupled nonlinear diffusion model by comparing it with the linear Fickian diffusion model (commonly used in the existing literature, see for example in Bi et. al.[9]).

Delithiation and Lithiation of a particle of diameter 2 μm and at a rate of 4C.—*Delithiation for* $H/d = 1$. —We start by exploring the effect of fast charging on the stress state. At the start of delithiation the cylindrical particle is assumed to have a uniform occupancy of 0.95. This value is chosen because in practice it is difficult to lithiate NMC particles fully unless they are held for long periods of time at low voltages, largely because Li transport is extremely sluggish at higher Li contents.[20,29,30] A fixed value of I_S was used corresponding to a delithiation rate of 4C and the current was switched off at $t = 15$ min. At this instant the particle is 'nominally delithiated' such that $\langle\theta\rangle = 0.2$, but the distribution of lithium is non-uniform (Fig. 2a). Lithium diffusion continues within the particle until it attains a uniform state of $\theta = 0.2$ as $t \to \infty$. We emphasize that positive values of the axial stress σ_c indicate tensile stresses.

Contours of lithium occupancy θ and of axial stress σ_c are shown side-by-side in Figs. 2(a) and 2(b), respectively. Recall that the particle is isolated with no mechanical constraint, and hence is free of external traction; the current is applied only on the curved surface of the particle at $r = 1$ μm. As a result of stress coupling, the occupancy close to the top and bottom free surfaces is altered by the traction-free boundary condition, see Fig. 2(a). The axial stress σ_c attains its extremum on the horizontal mid-plane of the particle at $z = 0$ and vanishes on the free surfaces $z = \pm 1$ μm, as demanded by the traction-free boundary condition, see Fig. 2(b). The main focus of the present study is to examine the possibility of tensile cracking in the

particle. The maximum values of circumferential and radial stresses are significantly smaller than the maximum values of axial stresses and hence not discussed here in detail. Moreover, plasticity can only occur due to slip on the **ab**-plane when the resolved shear stress σ_{rz} on that plane exceeds the shear strength of the NMC811 crystal. This strength has been reported to be 80 MPa[31]. Contours of shear stress σ_{rz} are given in Fig. 2(c) and are only non-vanishing near the upper and lower free surfaces. The peak stress of 100 MPa is localized in a small region while the shear stresses in the bulk of the crystal are well below the shear yield strength. Consequently, we do not expect plastic deformation of the crystal justifying our assumption of neglecting plasticity. This observation holds true throughout the simulation; accordingly, we focus attention on the mid-plane $z = 0$ and evaluate the radial variation of θ and σ_c at selected times, see Figs. 3(a) and 3(b).

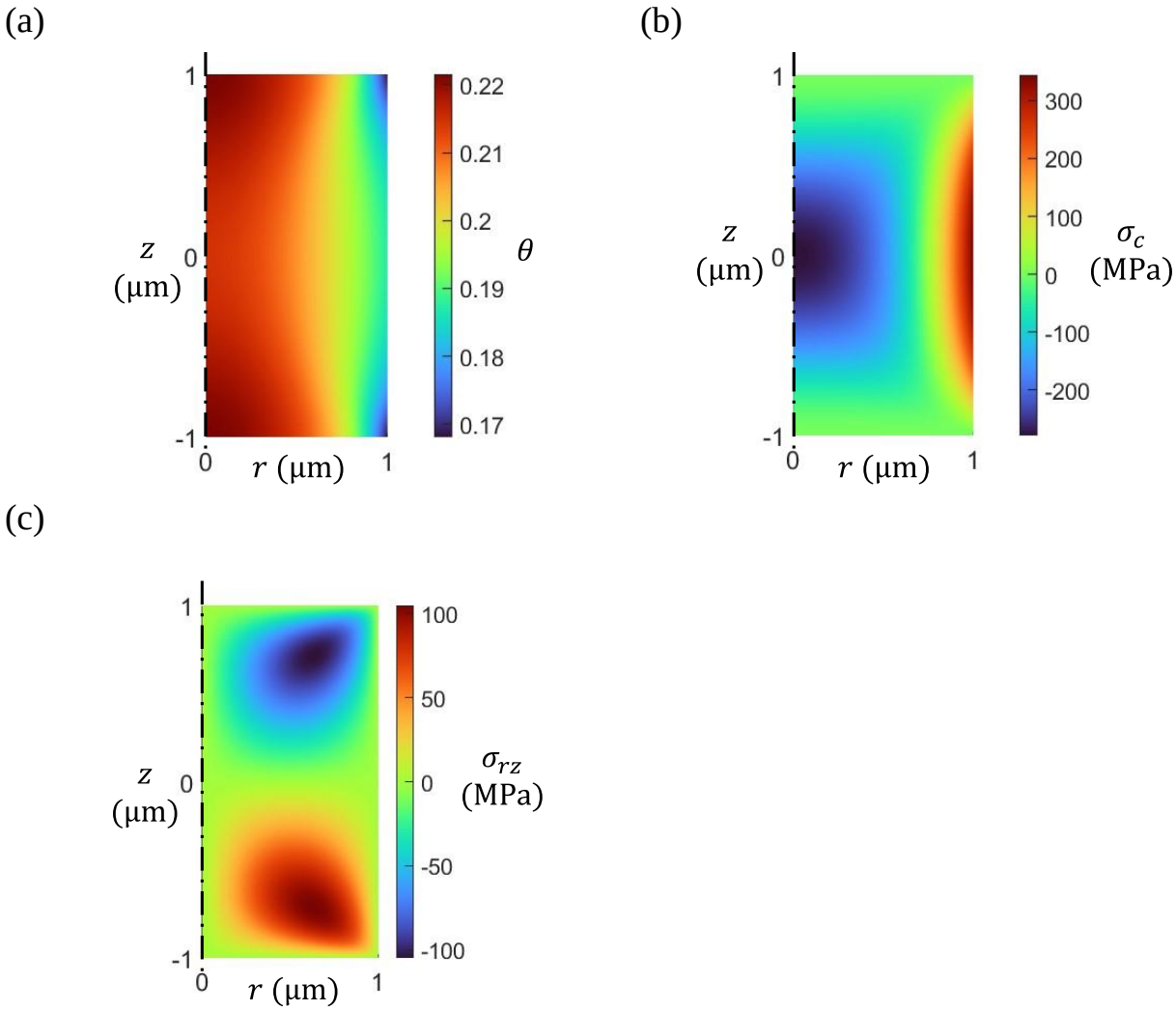

Figure 2. (a)-(c) predictions for a particle of diameter $d = 2$ μm *delithiated* at 4C. Contours of (a) θ, (b) σ_c and (c) σ_{rz} are plotted at $t = 15$ min.

At $t = 0$, the particle has a uniform occupancy and is stress-free. The low initial value of diffusivity in the vicinity of the fully lithiated state (recall Fig. 1(d)) limits diffusion inside the particle and a significant radial drop in θ is evident only near the surface of the particle at $t = 2$ min. The reduced occupancy near the surface leads to a larger lithiation strain ε_c^θ and to a compressive axial stress near the surface. Since the diffusivity increases by two orders when θ approaches 0.6 a nearly uniform particle occupancy exists at $t = 12$ min, and consequently a low level of stress exists in the particle. Subsequently, θ drops to below 0.37 at the surface, ε_c^θ decreases, and a tensile axial stress develops near the surface of the particle. The tensile axial stress σ_c achieves a maximum value on the mid-plane and either at the particle centre or at its surface (see Fig. 3(b)). The temporal variation of the mid-plane stress σ_c, at the particle centre ($r = 0$) and at the surface ($r = d/2$), are plotted in Fig. 3(c). This mid-plane stress attains a maximum value of 350 MPa at the surface when the delithiation current is switched-off. This peak value is associated with a highly nonlinear distribution of lithiation strain $\varepsilon_c^\theta(\theta)$ at the end of delithiation (15 min): recall from the characteristic of Fig. 1(b) that ε_c^θ decreases sharply from 3.5% to 0 when θ decreases from 0.3 to 0.1.

So far, results have been presented for the fully coupled chemo-mechanical model. In this formulation, the occupancy and state of stress are coupled through Eq. [22]. Despite the fact that the fully coupled formulation is a realistic representation of the evolution processes occurring in the cathode particle, additional insight into the influence of stress upon diffusion is achieved by considering the uncoupled problem where the stress coupling term in Eq. [22] is neglected. The evolution of lithium occupancy and axial component of stress are included as dashed lines in Figs. 3(a), 3(b) and 3(c). Until $t = 12$ min, the profiles of θ and σ_c as predicted by the uncoupled formulation, are indistinguishable from those of the fully-coupled formulation. In contrast, at $t = 15$ min, the difference in stress predictions is significant but not that of θ. In particular, at $t = 15$ min, the axial stress $\sigma_c = 900$ MPa is large at the particle surface for the uncoupled case, see Fig. 3(c). Note that, this stress is significantly higher than the coupled case. A minor difference ($\Delta\theta \approx 0.02$) in the predictions of surface occupancies between the two formulations correspondingly leads to lithiation strain difference of 0.3%. The high sensitivity of lithiation strains to the occupancy combined with a large elastic modulus $E_z = 164$ GPa (calculated from Table 2) gives rise to the additional 550 MPa for the uncoupled case.

We explain this behaviour as follows. The occupancy at $t = 12$ min is almost uniform in the radial direction on the mid-plane and is positioned at the peak of the lithiation characteristic for ε_c^θ in Fig. 1(b). A small drop in occupancy leads to a major change in ε_c^θ, and if this major drop in ε_c^θ varies radially then it is accompanied by a large change in axial stress. This is the case for the uncoupled model, as evidenced by the axial stress profile at $t = 15$ min in Fig. 3(b). When stress coupling is activated in the model, the compressive stress at the particle centre drives the lithium ions towards the surface as demanded by the flux law Eq. [22], thereby reducing the gradient $\partial\theta/\partial r$. We conclude that an attempt to simplify the model by eliminating the stress contribution can lead to an over-prediction of the maximum stresses generated in the particle.

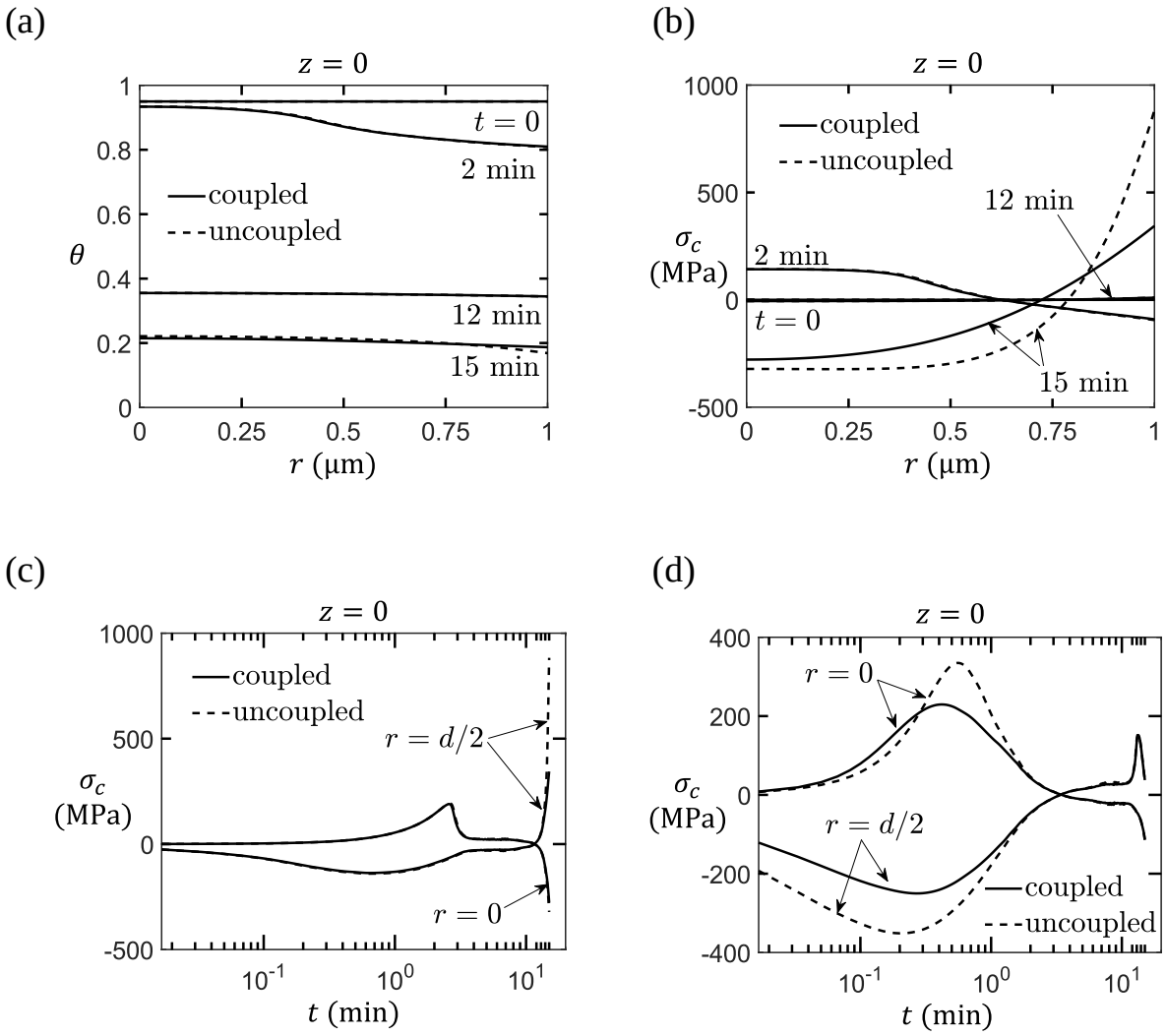

Figure 3. (a)-(c) predictions for a particle of diameter $d = 2$ μm *delithiated* at 4C. The radial variation of (a) θ and (b) σ_c are plotted on the mid-plane ($z = 0$) at selected times; (c) time evolution of σ_c at the centre $r = 0$ and at the surface $r = d/2$. (d) time evolution of σ_c at the

centre $r = 0$ and at the surface $r = d/2$, for a particle of diameter $d = 2$ μm *lithiated* at 4C.

Lithiation for $H/d = 1$.—Lithiation at an imposed rate of 4C for 15 min takes the particle from a uniform state of $\theta = 0.2$ to a 'fully lithiated' state of $\langle\theta\rangle = 0.95$, and after the current has been switched off, diffusion continues until equilibrium is reached and the occupancy becomes uniform at $\theta = 0.95$.

A set of predictions for lithiation of a finite cylinder with $H/d = 1$ is given in Fig. A1 of Appendix A for both the coupled and uncoupled models. A side-by-side comparison of the delithiation and lithiation cases is given in Figs. 3(c) and (d), respectively: the axial stress on the mid-plane at the particle centre and surface is plotted as a function of time. The peak tensile axial stress generated by lithiation occurs at the centre of the particle for both the coupled and uncoupled models; the peak value equals 333 MPa for the uncoupled model, and 230 MPa for the coupled model. These values are somewhat lower than those generated by delithiation, compare Figs. 3(c) and 3(d).

Why is the peak stress for lithiation achieved much sooner (after 1 min) than the peak stress for delithiation (after 15 min)? The answer lies in the fact that the maximum slope of the $\varepsilon_c^\theta(\theta)$ characteristic occurs in the regime $0.1 \leq \theta \leq 0.3$. Values of occupancy in this regime occur early in lithiation, and late in delithiation.

Effect of particle aspect ratio H/d *upon axial stress during lithiation and delithiation.*—For the particle of diameter 2 μm, the maximum tensile stress $\sigma_c^{\max}$ on the particle mid-plane is plotted as a function of aspect ratio in the range $H/d = 0.5$ to 2.5, see Fig. 4(a) for delithiation and Fig. 4(b) for lithiation. The peak axial stress increases with increasing aspect ratio H/d for both lithiation and delithiation. Delithiation of a long particle generates the highest value of axial stress (361 MPa), and this occurs at the surface of the particle.

We proceed to predict upper-bound values of axial stress for selected values of particle diameter and C-rate by analysing the lithiation and delithiation responses of a circular cylinder of infinite length, $H/d \to \infty$. The assumption of infinite length reduces the 2D axisymmetric problem for a finite particle to a 1D problem of a circular cylinder under generalised plane

strain in the axial direction. The axial strain ε_{zz} is spatially uniform and is of magnitude $\varepsilon_0(t)$ such that the axial force F_c vanishes. Consequently, the axial stress σ_c satisfies the condition

$$F_c = 2\pi \int_0^{\frac{d}{2}} \sigma_c(r,t)\, r dr = 0, \qquad [33]$$

and the work-conjugate axial strain $\varepsilon_0(t)$ becomes a solution variable to enforce Eq. [33]; see Appendix B where we demonstrate the uniqueness of ε_0. The problem reduces to a one-dimensional (1D) analysis in the spatial variable r and time t, and the boundary conditions reduce to: (i) the radial ionic flux $j_r = I_S/F$ on $r = d/2$ and (ii) the radial component of stress $\sigma_{rr} = 0$ on $r = d/2$. Similarly, in the other extreme of $H/d \to 0$, the problem becomes one of plane stress and is 1D in r such that $\sigma_c = 0$ for all r (and all t).

Simulations have been performed using the coupled model for the case of plane stress, ($H/d \to 0$), and for generalised plane strain ($H/d \to \infty$), for both lithiation and delithiation at a rate of 4C. Remarkably, the distribution of occupancy in the limits of plane stress and generalised plane strain are the same as that observed for $H/d = 1$ (to within 1%); the occupancy for $H/d = 1$ has already been reported in Fig. 3(a) for delithiation, and in Fig. A1(c) for lithiation. The axial stress is sensitive to the radial distribution of ε_c^θ and there is a small dependence of the ε_c^θ profile upon the aspect ratio of the particle. Consequently, the axial stress distribution for the infinite cylinder is slightly different from that of the finite particle of $H/d = 1$, see Fig. 4(c) for delithiation and Fig. 4(d) for lithiation. The traction-free boundary conditions dictate that the axial stress vanishes in the plane stress limit. In broad terms, we conclude that the generalised plane strain solution for $H/d \to \infty$ gives an accurate prediction for the axial stress distributions for H/d of unity and above. The above calculations also imply that the storage response is relatively insensitive to particle aspect ratio over the full range from zero to infinity.

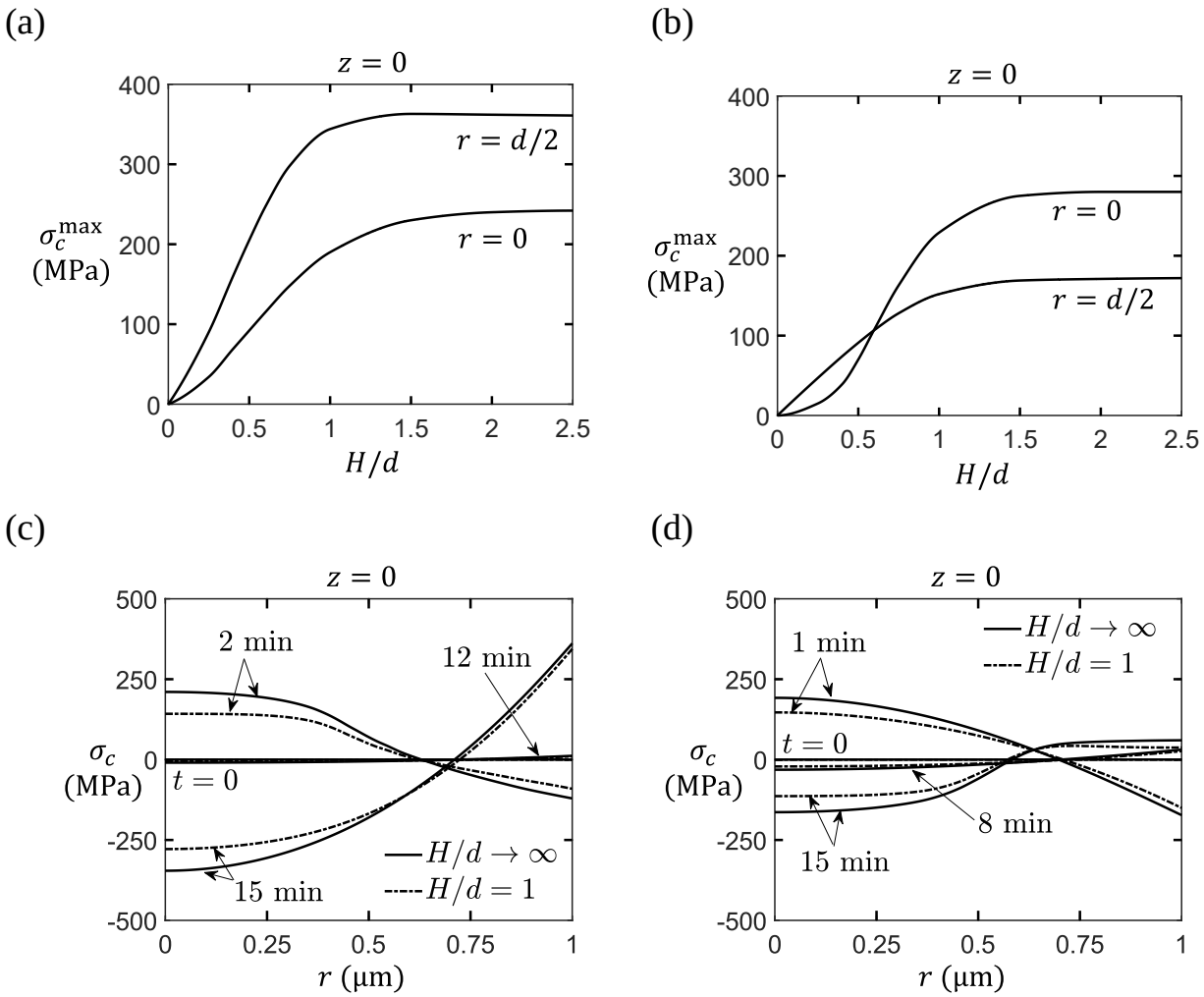

Figure 4. Effect of particle aspect ratio H/d on $\sigma_c^{\max}$ for (a) delithiation and (b) lithiation. Axial stress σ_c distribution on the mid-plane for $H/d = 1, \infty$ during (c) delithiation and (d) lithiation. In all cases, a rate of 4C is imposed on a particle of diameter 2 μm, and predictions are given by the coupled, nonlinear model.

Assessment of particle cracking and safe operation regimes.−The possibility of tensile cracking due to an axial tensile stress is now explored in an approximate manner by assuming that a surface-breaking thumbnail-shaped crack of depth a_0 and width c_0 exists on a transverse section of the particle, recall Fig. 1(a). In addition, an embedded penny-shaped crack of radius a_0 exists at the centre of the particle, again on a transverse plane.

We begin by plotting stress maps that give contours of maximum axial tensile stress $\sigma_c^{\max}$ over all time, as a function of particle diameter d and C-rate n for the case $H/d \to \infty$, see Fig. 5. Predictions are given for the peak tensile axial stress $\sigma_c^{\max}$ at the surface and at the centre for delithiation in Fig. 5(a) and for lithiation in Fig. 5(b). For all four cases of

delithiation/lithiation and surface/centre shown in Fig. 5, $\sigma_c^{\max}$ increases with increasing particle size and increasing C-rates. For any combination of d and n, $\sigma_c^{\max}$ is greatest at the surface during delithiation and at the particle centre during lithiation.

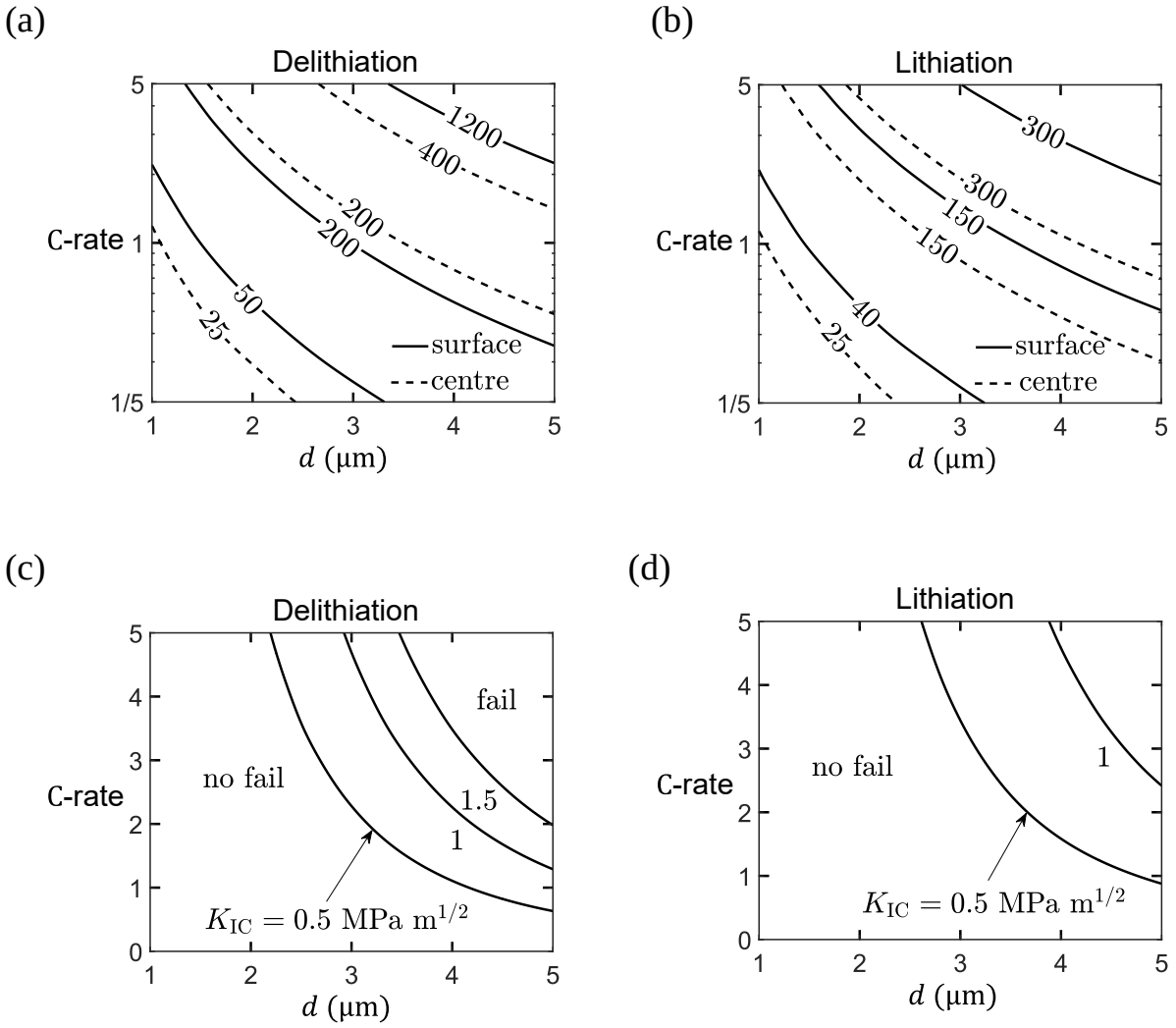

Figure 5. Contours of maximum tensile stress $\sigma_c^{\max}$ (in the units of MPa) during (a) delithiation and (b) lithiation as a function of particle diameter d and C-rate. The boundary between the no-fail region and the fail region is shown for (c) delithiation with $K_{\mathrm{IC}} = 0.5 - 1.5$ MPa m$^{1/2}$. (d) For lithiation we show these results with $K_{\mathrm{IC}} = 0.5 - 1.0$ MPa m$^{1/2}$. No failure is predicted over the full range of particle diameter d and C-rate considered for the choice $K_{\mathrm{IC}} = 1.5$ MPa m$^{1/2}$. A representative size of $a_0 = d/8$ and $c_0 \approx a_0$ (see Figure 1(a)) has been assumed for a pre-existing thumbnail crack in Figure (c). Similar, a representative size of $a_0 = d/8$ has been assumed for the penny-shaped centre-crack in Figure (d).

The above predictions of axial stress can be used to estimate the likelihood of cleavage fracture from defects aligned with the basal plane as shown in Fig. 1(a). Consider the worst-

case aspect ratio of $H \gg d$ which gives an upper bound $\sigma_c^{\max}$. For a given particle diameter d and value n of C-rate we explore whether the predicted value of $\sigma_c^{\max}(d,n)$ is sufficient to induce cleavage fracture from a pre-existing crack of size a_0.

Fracture mechanics teaches us that the mode I stress intensity factor K_{I} for a plane strain crack of length $2a$ in an infinite solid under a uniform remote stress σ is $K_{\mathrm{I}} = \sigma\sqrt{\pi a}$. In the present problem, the stress distribution is not uniform and the crack plane occupies a finite fraction of the cross-section. In the present study we assume a representative value of $a_0 = d/8$. Additionally, the stress intensity factor varies along the periphery of the thumbnail crack and depends upon c_0 in addition to a_0. For the present purposes, we shall use the simplified formula $K_{\mathrm{I}} = \sigma^{\max}\sqrt{\pi a_0}$ and assume that c_0 is comparable to a_0 for the thumbnail crack case. Thus fracture occurs at a stress $\sigma_c^{\max}$ that satisfies $K_{\mathrm{IC}} = \sigma_c^{\max}\sqrt{\pi a_0}$, where K_{IC} is the mode I fracture toughness of the solid. Then, a region of safe operation can be demarcated over the variables n and d as shown in Figs. 5(c) and 5(d) for selected values of K_{IC} in the range of 0.5 MPa $\mathrm{m}^{1/2}$ to 1.5 MPa $\mathrm{m}^{1/2}$, which are typical for cathodic materials. The above simple estimates suggest that single-crystals of diameter up to 2.5 μm (and pre-existing flaws of dimension $a_0 = d/8$) are not prone to cracking up to fast C-rates of 5C. The operating regime to avoid fracture is more restricted with diminishing fracture toughness. Larger particles will crack, particularly at high C-rates.

Effect of the uncertainty of the non-linear parameters.—There is considerable uncertainty in the measured lithiation strains and the occupancy-dependent diffusion coefficients, recall Figs. 1(b) and 1(d). To investigate the effect of this uncertainty on our predictions consider, by way of example, delithiation of a single crystal in the form of a circular cylinder of diameter 2 μm and infinite height. A rate of 4C is imposed such that $\langle\theta\rangle$ drops from 0.95 to 0.2 in 15 min. The resulting occupancies at the centre and surface of the particle are plotted as a function of time in Figs. 6(a) and 6(b), respectively, for the coupled, nonlinear model using the parameters taken from Refs. 24,27. The predictions of occupancy are not strongly affected by the uncertainty in the data.

Next, consider additional predictions of axial stress at the centre and surface of the particle on the basis of Refs. 24,27, see Figs. 6(c) and 6(d). The difference between two sets of predictions is greater for axial stress than it is for occupancy. This discrepancy arises primarily

because the stress-state is strongly dependent upon the intercalation strain and the differences between the intercalation strain measurements in Märker et al.[21] and Biasi et al.[24] are substantial, as shown in Fig. 1(b).

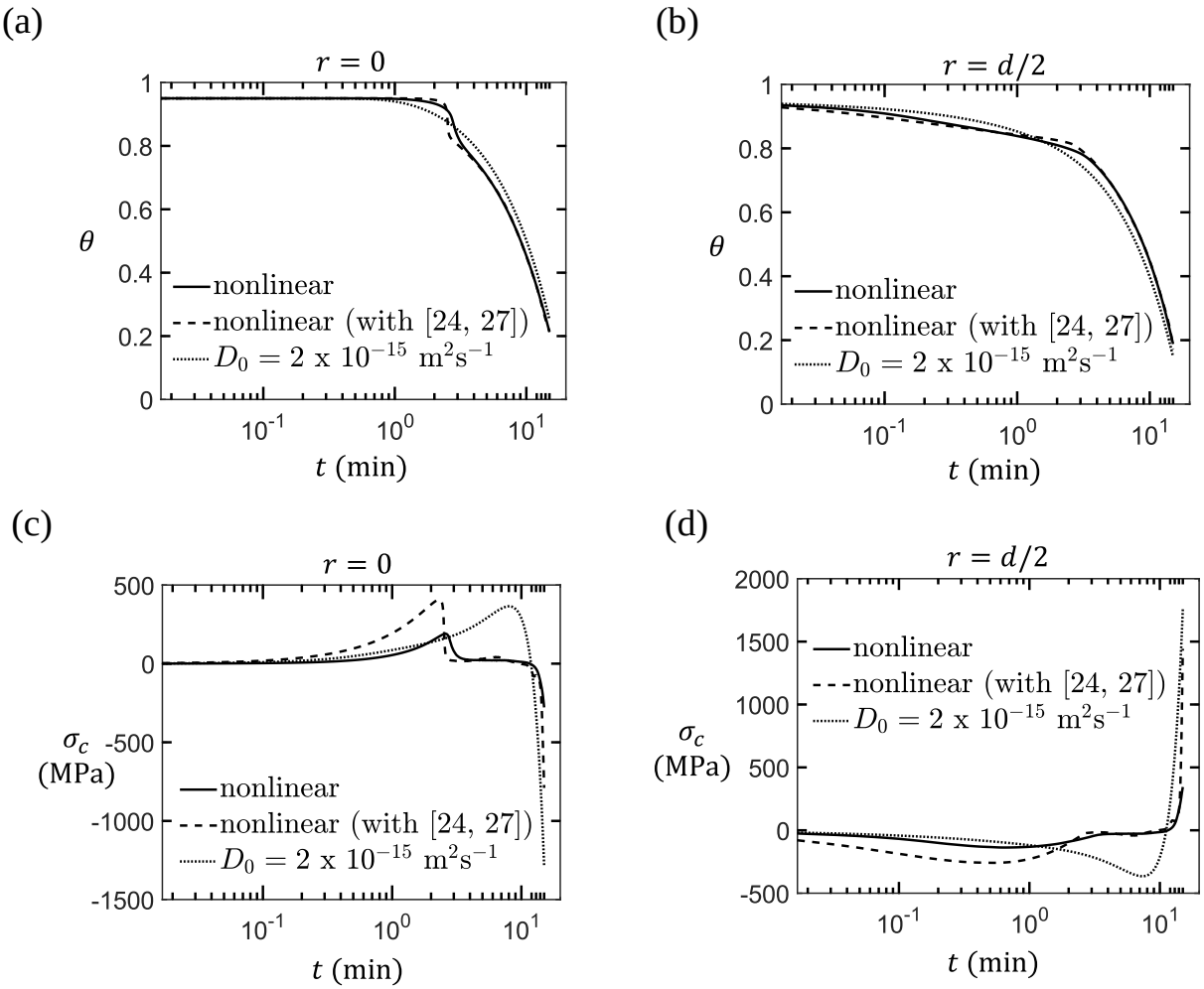

Figure 6. Comparison of linear and nonlinear models for delithiation of a particle of infinite length and diameter 2 μm at a rate of 4C. Time evolution of θ at (a) centre, $r = 0$ and (b) surface, $r = d/2$. Time evolution of σ_c at (c) centre, $r = 0$ and (d) surface, $= d/2$.

Comparison with linear Fickian diffusion.−Commonly in the literature (for example Bi et al.[9]) the transient distribution of occupancy within a single crystal is predicted by assuming linear Fickian diffusion of the lithium, with stress playing no role. The Fickian diffusion equation for a circular cylindrical particle of infinite length reads

$$\frac{\partial N_{\mathrm{Li}^+}}{\partial t} = N_L D_0 \left(\frac{\partial^2 \theta}{\partial r^2} + \frac{1}{r} \frac{\partial \theta}{\partial r} \right). \qquad [34]$$

in terms of a constant diffusion coefficient D_0. Recall from Fig. 1(d) that the diffusivity varies with occupancy by more than 2 orders of magnitude, and so the use of linear Fickian diffusion theory is questionable. Additionally, lithium diffusion is driven by enthalpic forces (as evidenced by the strong dependence of open circuit voltage upon occupancy). It is concluded that traditional approaches neglect major nonlinearities in the diffusivity and in the driving force for diffusion.

A direct comparison is now made between the full nonlinear model of the current study and linear Fickian diffusion. Predictions of the occupancy with Fickian diffusion for $D_0 = 2 \times 10^{-15}\ \mathrm{m^2 s^{-1}}$ are included in Figs. 6(a) and 6(b). The corresponding predictions of the axial stress using the occupancies predicted by the Fickian diffusion are given in Figs. 6(c) and 6(d) using the intercalation strains from Märker et al.[21]. The overall conclusion is that a Fickian diffusion model with $D_0 \approx 2 \times 10^{-15}\ \mathrm{m^2 s^{-1}}$ suffices to capture the occupancy within the particle although the stress predictions are prone to errors due to the strong sensitivity of ε_c^{θ} to the occupancy at low levels of occupancy. The error in stress prediction using the Fickian model is within the uncertainty associated with the non-linear parameters: compare stress predictions using the two sets of non-linear parameters in Figs. 6(c) and 6(d). The above conclusions for the accuracy of the linear Fickian model have been confirmed for a range of C-rates and particle sizes.

Concluding Remarks

Quantitative predictions are made for the peak stresses generated in storage particles of NMC811 single crystal during battery operating conditions. By making use of a chemo-mechanical model for lithium diffusion and stress evolution in isolated single particles of realistic size, we have shown that the likelihood of particle fracture due to lithium diffusion is minimal. The current work suggests that the cracks reported in the literature may have resulted from external stress on the particles and that an unconstrained single crystal of diameter less than 2.5 μm will not crack at rates of up to 5C. The present work suggests that intraparticle fracture is not a significant degradation mode for well-designed NMC811 single crystals. Future work is needed to examine Ni-rich cathode materials of Ni content exceeding 80%, where a degradation mode has been proposed for the increased capacity fade rates of Ni-rich cathode materials, whether they are single crystal or polycrystalline.[5]

The present study has highlighted that lithium diffusion in single crystals involves the non-linear dependence of (i) diffusivity, (ii) open circuit voltage and (iii) lithiation strain upon lithium occupancy. Our study reveals that the cross-coupling between diffusion rate and stress state is minor. Consequently, an uncoupled, non-linear diffusion model suffices for prediction of the distribution of occupancy at any instant; the calculation of stress state can then be performed as a post-processing step provided the intercalation strain is not overly sensitive to occupancy. Moreover, we show that an appropriately calibrated Fickian diffusion model suffices to predict the occupancy within the particle. Predictions of stress by the Fickian model are within the errors associated with uncertainty in the measurements of intercalation strain.

Acknowledgements

This work was supported by the Faraday Institution Degradation Project [grant numbers FIRG001 and FIRG024]. N.A.F acknowledges funding from the European Research Council in the form of an Advanced Grant (MULTILAT, 669764). C.P.G. acknowledges support from an ERC Advanced Investigator Grant (EC H2020 ERC 835073).

Author Contributions

S. S. Pandurangi: Conceptualization, Methodology, Software, Formal Analysis, Writing – original draft. **D. S. Hall:** Funding acquisition, Project administration, Writing – Review and editing, **C. P. Grey:** Funding acquisition, Supervision, Project administration, Writing – Review and editing**, V. S. Deshpande:** Conceptualization, Methodology, Supervision, Project administration, Writing – Review and editing. **N. A. Fleck:** Conceptualization, Methodology, Supervision, Project administration, Writing – Review and editing.

References

1. G. E. Blomgren, *J. Electrochem. Soc.*, **164**, A-5019 (2017).
2. A. Koyamparambath, J. Santillán-Saldivar, B McLellan, and G Sonnemann, *Resources Policy*, **75**, 102465 (2022).
3. E. A. Olivetti, G. Ceder, G. G. Gaustad, and X. Fu, *Joule*, **1**, 229 (2017).
4. S.-T. Myung, F. Maglia, K.-J. Park, C. S. Yoon, P. Lamp, S.-J. Kim, and Y.-K. Sun, *ACS Energy Lett.*, **2**, 196 (2017).

5. H. Li, A. Liu, N. Zhang, Y. Wang, S. Yin, H. Wu, and J. R. Dahn, *Chem. Mater.*, **31**, 7574 (2019).
6. H.-H. Ryu, K.-J. Park, C. S. Yoon, and Y.K. Sun, *Chem. Mater.*, **30**, 1155 (2018).
7. J. E. Harlow, X. Ma, J. Li, E. Logan, Y. Liu, N. Zhang, L. Ma, S. L. Glazier, M. M. E. Cormier, M. Genovese, S. Buteau, A. Cameron, J. E. Stark, and J. R. Dahn, *J. Electrochem. Soc.*, **166**, A3031 (2019).
8. S. Li, Z. Jiang, J. Han, Z. Xu, C. Wang, H. Huang, C. Yu, S.-J. Lee, P. Pianetta, H. Ohldag, J. Qiu, J.-S. Lee, F. Lin, K. Zhao, and Y. Liu, *Nat. Commun.*, **11**, 4433 (2020).
9. Y. Bi, J. Tao, Y. Wu, L. Li, Y. Xu, E. Hu, B. Wu, J. Hu, C. Wang, J.-G. Zhang, Y. Qi, and J. Xiao, *Science*, **370**, 1313 (2020).
10. G. Qian, Y. Zhang, L. Li, R. Zhang, J. Xu, Z. Cheng, S. Xie, H. Wang, Q. Rao, Y. He, Y. Shen, L. Chen, M. Tang, and Z.-F. Ma, *Energy Storage Mater.*, **27**, 140 (2020).
11. S. Lee, W. Jin, S. H. Kim, S. H. Joo, G. Nam, P. Oh, Y.-K. Kim, S. K. Kwak, and J. Cho, *Angew. Chem. Int. Ed.*, **58**, 10478 (2019).
12. Y. Liu, J. Harlow, and J. Dahn, *J. Electrochem. Soc.*, **167**, 020512 (2020).
13. X. Zhang, W. Shyy, and A. M. Sastry, *J. Electrochem. Soc.*, **154**, A910 (2007).
14. R. Purkayastha and R. McMeeking, *Comput. Mater. Sci.*, **80**, 2-14 (2013).
15. R. Purkayastha and R. McMeeking, *Meccanica*, **51**, 3081 (2016).
16. K. Zhao, M. Pharr, J. J. Vlassak, and Z. Suo, *J. Appl. Phys.*, **108**, 073517 (2010).
17. N. Nadkarni, T. Zhou, D. Fraggedakis, T. Gao, and M. Z. Bazant, *Adv. Funct. Mater.*, **29**, 1902821 (2019).
18. N. Nadkarni, E. Rejovitsky, D. Fraggedakis, C. V. D. Leo, R. B. Smith, P. Bai, and M. Z. Bazant, *Phys. Rev. Mater.*, **2**, 085406 (2018).
19. K. Yang and M. Tang, *J. Mater. Chem. A.*, **8**, 3060 (2020).
20. C. Xu, A. J. Merryweather, S. S. Pandurangi, Z. Lun, D. S. Hall, V. S. Deshpande, N. A. Fleck, C. Schnedermann, A. Rao, and C. P. Grey, *Joule*, **6**, 2535 (2022).
21. K. Märker, P. J. Reeves, C. Xu, K. J. Griffith, and C. P. Grey, *Chem. Mater.*, **31**, 2545 (2019).
22. E. R. Logan, D. S. Hall, M. M. E. Cormier, T. Taskovic, M. Bauer, I. Hamam, H. Hebecker, L. Molino, and J. R. Dahn, *J. Phys. Chem. C*, **124**, 12269 (2020).
23. L. Onsager, *Phys. Rev.*, **38**, 2265 (1931).
24. L. d. Biasi, A. O. Kondrakov, H. Geßwein, T. Brezesinski, P. Hartmann, and J. Janek, *J. Phys. Chem. C*, **121**, 26163 (2017).
25. L. Onsager, Phys. Rev., **37**, 405 (1931).

26. R. Böhmer, K. R. Jeffrey, and M. Vogel, *Prog. Nucl. Magn. Reson. Spectrosc.*, **50**, 87 (2007).
27. E. Trevisanello, R. Ruess, G. Conforto, F. H. Richter, and J. Janek, *Adv. Energy Mater.*, **11**, 2003400 (2021).
28. A. F. Bower and P. R. Guduru, Modelling. *Simul. Mater. Sci. Eng.*, **20**, 045004 (2012).
29. A. Grenier, P. J. Reeves, H. Liu, I. D. Seymour, K. Märker, K. M. Wiaderek, P. J. Chupas, and C. P. Grey, K. W. Chapman, *J. Am. Chem. Soc.*, **142**, 7001 (2020).
30. J. Park, H. Zhao, S. D. Kang, K. Lim, C.-C. Chen, Y.-S. Yu, R. D. Braatz, D. A. Shapiro, J. Hong, M. F. Toney, M. Z. Bazant, and W. C. Chueh, *Nat. Mater.*, **20**, 991 (2021).
31. J. C. Stallard, S. Vema, D. S. Hall, A. R. Dennis, M. E. Penrod, C. P. Grey, V. S. Deshpande, and N. A. Fleck, *J. Electrochem. Soc.*, **169**, 040511 (2022).

Appendix A

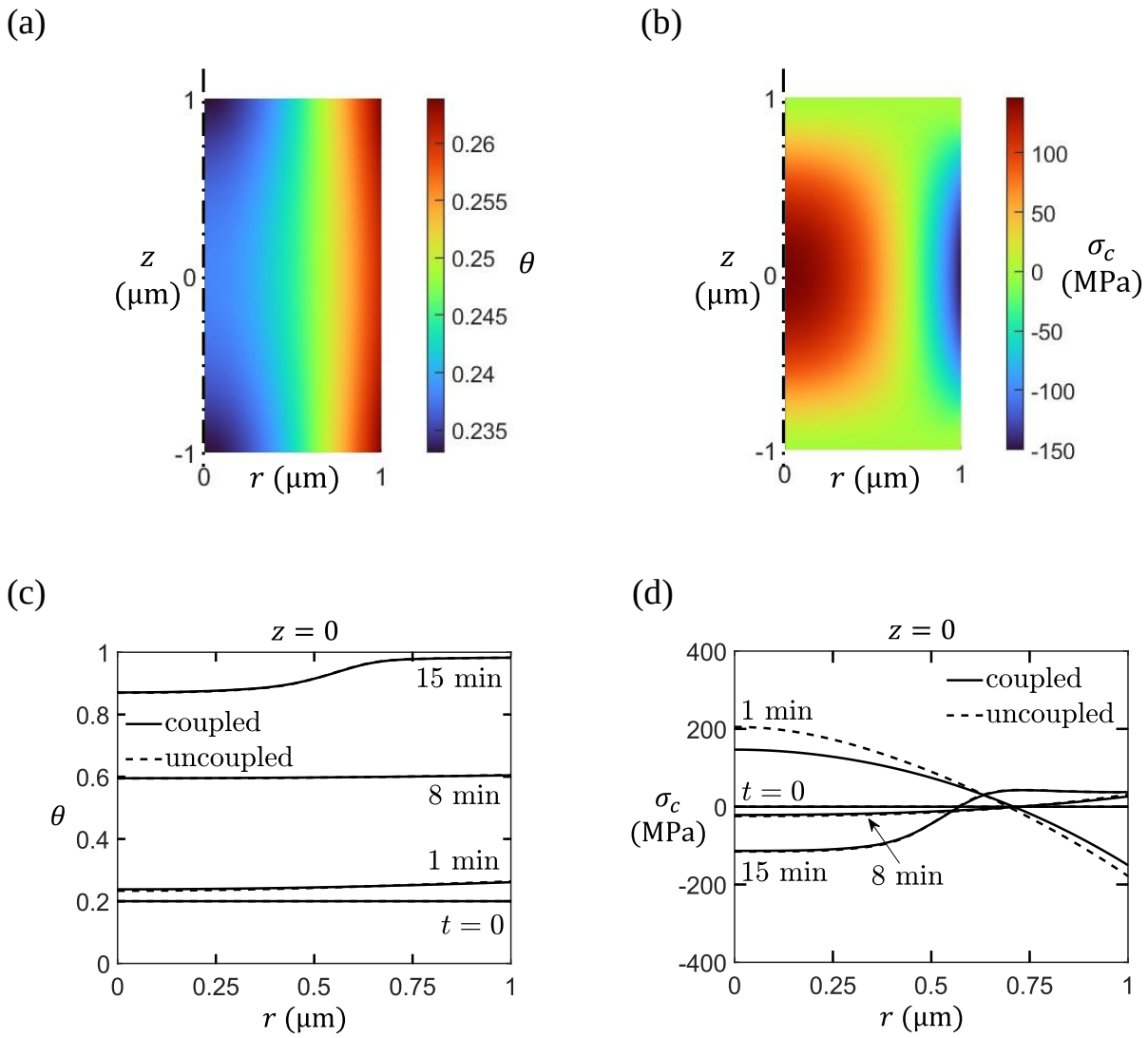

Figure A1. Contours of (a) θ and (b) σ_c at $t = 1$ min for a particle of diameter $d = 2$ μm *lithiated* at 4C. The radial variation of (c) θ and (d) σ_c on the mid-plane ($z = 0$) is plotted at selected times.

Appendix B

Derivation of $\varepsilon_0(t)$

From the constitutive relation Eq. [5] we know that $\varepsilon_0(t)$ satisfies,

$$\varepsilon_0 = \left[\frac{1}{E_z}\sigma_c - \frac{\nu_{rz}}{E_z}(\sigma_{rr} + \sigma_{\omega\omega})\right] + \varepsilon_c^{\theta}. \qquad [B\cdot1]$$

On integrating Eq. [B·1] over the **ab**-plane we get,

$$\int_0^{\frac{d}{2}} \varepsilon_0 \; rdr \; = \frac{1}{E_z}\int_0^{\frac{d}{2}} \sigma_c \; rdr - \frac{\nu_{rz}}{E_z}\int_0^{\frac{d}{2}} (\sigma_{rr} + \sigma_{\omega\omega}) \; rdr + \int_0^{\frac{d}{2}} \varepsilon_c^{\theta} \; rdr. \qquad [B\cdot2]$$

At any given instant t, ε_0 is spatially uniform and the first integral on the right-hand-side of Eq. [B·2] vanishes due to Eq. [33]. Equation [B·2] can then be written as,

$$\varepsilon_0 \; = -\frac{\nu_{rz}}{E_z}\langle\sigma_{rr} + \sigma_{\omega\omega}\rangle + \langle\varepsilon_c^{\theta}\rangle. \qquad [B\cdot3]$$

where $\langle\cdot\rangle$ denotes a volume-averaged quantity.

We will now show that $\langle\sigma_{rr} + \sigma_{\omega\omega}\rangle = 0$.

$$\langle\sigma_{rr} + \sigma_{\omega\omega}\rangle = \frac{8}{d^2}\int_0^{\frac{d}{2}} (\sigma_{rr} + \sigma_{\omega\omega}) \; rdr. \qquad [B\cdot4]$$

The equilibrium equation Eq. [26] for axis-symmetric problem yields,

$$\frac{d\sigma_{rr}}{dr} + \frac{(\sigma_{rr} - \sigma_{\omega\omega})}{r} = 0 \Rightarrow \sigma_{\omega\omega} = r\frac{d\sigma_{rr}}{dr} + \sigma_{rr}. \qquad [B\cdot5]$$

On substituting Eq. [B·5] into [B·4] we get,

$$\langle\sigma_{rr} + \sigma_{\omega\omega}\rangle = \frac{8}{d^2}\left[\int_0^{\frac{d}{2}} r^2\frac{d\sigma_{rr}}{dr} \; dr + \int_0^{\frac{d}{2}} 2r\sigma_{rr} \; dr\right]. \qquad [B\cdot6]$$

Finally, on integrating the first integral by parts, the Eq. [B·6] can be written as

$$\langle\sigma_{rr} + \sigma_{\omega\omega}\rangle = \frac{8}{d^2}(r^2\sigma_{rr})\Big|_0^{d/2} = 2\sigma_{rr}(d/2). \qquad [B\cdot7]$$

As the particle-surface is traction-free, $\sigma_{rr}(d/2) = 0$. Therefore, $\langle\sigma_{rr} + \sigma_{\omega\omega}\rangle = 0$.

It can be concluded from Eq. [B·3] that there is a unique value of the total **c**- axis strain ε_0 specified by

$$\varepsilon_0(t) \; = \langle\varepsilon_c^{\theta}\rangle, \qquad [B\cdot8]$$

which satisfies the constraint Eq. [33] at any given time t.